IOSR Journal of Applied Geology and Geophysics (IOSR-JAGG)
e-ISSN: 2321–0990, p-ISSN: 2321–0982. Volume 13, Issue 4 Ser. I (July – August 2025), PP 01-17
www.iosrjournals.org

Anisotropic Shear Strength, Wave Velocity And Permeability Characteristics Of Freiberg Gneiss Under Hydrostatic And Triaxial Deformations

Bernard Adero
Ruhr University Bochum, Institute Of Geology, Mineralogy And Geophysics, Germany
Now At: National Defence University-Kenya, P.O BOX, 370, Nakuru Kenya

Abstract
The crystalline Freiberg gneiss is anisotropic in its hydraulic properties, shear and tensile failure, and wave velocity propagational behaviour. Its anisotropy depends not only on the magnitude of the principal stresses, but also on the foliation orientations relative to the principal stresses. In this study, the hydraulic and mechanical anisotropies are investigated in the laboratory under hydrostatic and triaxial stress conditions in order to aid the interpretation of the field hydraulic stimulation for in-situ stress measurements conducted in boreholes drilled in the underground research mine in Freiberg mine, Germany. The pore-pressure oscillatory hydraulic tests and velocity measurements were investigated under hydrostatic stress conditions representative of stresses in the mine, subsequently, triaxial deformation tests with simultaneous ultrasonic velocity measurements, were performed on the rocks recovered from the Freiberg mine and cored in different orientations relative to the visible foliation. Triaxial compression tests revealed significantly higher compression strength when samples were loaded normal to the foliation compared to when the samples were loaded parallel to the foliation, indicating considerable mechanical strength anisotropy. Freiberg gneiss exhibit estimated average compressional and shear velocity anisotropy values of 10 % and 19 %, respectively, and this anisotropy changes minimally (0.2 %) over the range of confining stresses investigated during hydrostatic tests. The axial oscillatory pore-pressure permeability measurements revealed that samples loaded parallel to the foliation exhibit higher permeability (~10^{-19} m^2) than the permeability of samples loaded normal to the foliation (~10^{-20} m^2) by an order of magnitude. This permeability does not significantly change with increasing effective pressure.

Keywords: *Anisotropy, permeability, velocity, shear strength*

Date of Submission: 09-07-2025 Date of Acceptance: 19-07-2025

I. Introduction

The rock masses are often under stresses and forces which in turn influence the mechanical stability of the rock materials. These imposed stresses and forces induce changes in the rock structures and form discontinuities in the rock masses. The foliation (planes of anisotropy) are classified as discontinuities in addition to fractures, joints, bedding planes, shear zones, faults, e.t.c (Ismael et al., 2014). From the perspective of rock mechanics, anisotropic nature of rocks causes the difference of the rock compressive strength, Young's modulus, and Poisson's ratio relative to the orientation of loading of the major principal stress and foliation (e.g. Ismael, 2014; Niandou et al., 1997; Saroglou & Tsiambaos, 2008; Sayers, 2013). Earlier authors (e.g. Donath, 1961; Jaeger et al., 2007; Walsh & Brace, 1964) investigated the effect of rock strength on the orientation of the foliation relative to the loading direction of the major principal stress and with increasing confining stresses. At low confining stresses, the rock undergoes a significant reduction in strength when the foliation becomes nearly aligned at about 30° to the axis of major principal stress. The rock strength is notably increased as the confining stress is increased because the rock is more readily predisposed to respond in a ductile manner, and the strength influence of the foliation, when at optimum orientation for early shear, is correspondingly reduced.

Elastic anisotropy is the variation of elastic properties with direction. The elastic anisotropy of rocks is an important geophysical parameter that can be used to classify rocks in petrophysical studies, to interpret seismic field measurements, and also to study the structure of the crust and the upper mantle of the earth. Elastic anisotropy occurs if there is a preferred alignment of a material's fabric elements such as, crystals, grains, cracks, bedding planes, joints or fractures, on a scale smaller than the length of the wave and by the combined action of the mentioned factors affected by external conditions, mainly stress-state conditions. This alignment causes waves to propagate fastest in its direction. The sensitivity of seismic velocity on stress has been studied

and reported for a variety of rocks by laboratory ultrasonic elastic wave velocity measurements in samples with varying pressures in their pore fluid (e.g. Sarout & Guéguen, 2008; Terzaghi, 1943).

Permeability of rocks is of immense concern in geophysical applications, for example, in hydrocarbon production, nuclear waste disposal, and in enhanced geothermal systems. Permeability is responsible for reservoir production (e.g. Fryer et al., 2019; Hofmann et al., 2014; Marek, 1979; Tester et al., 2006), and selection of nuclear disposal sites (Bradehoeft et al., 1978; Zharikov et al., 2014). For instance, in enhanced geothermal systems, hydraulic stimulation of the reservoir creates artificial fracture networks thereby leading to increased changes in permeability for geothermal heat extraction. Subsequently, fluid withdrawal from the reservoir leads to an increase in effective normal stresses resulting to a decreased change in permeability. These changes are of great concern to geoscientists and geophysical engineers. Specifically, knowledge of permeability changes is important during different production cases when dealing with reservoirs prone to pore collapse. Reductions in permeability may result in a decrease of ultimate recovery, reservoir compaction, and subsidence (Suri et al., 1997). There is significant difference between rock fracture permeability and rock matrix permeability. An approach to understanding matrix permeability is to study intact samples at the laboratory scale. Published permeability values of different rock types vary by several orders of magnitude and depend on the applied effective stress and the orientation of bedding or foliation relative to the flow direction (parallel or normal to foliation) (Armitage et al., 2011; Baud et al., 2012; Benson et al., 2006; Benson et al., 2005; Bhandari et al., 2015; David et al., 2001; Gehne & Benson, 2017). Moreover, initial rock permeability is one of the factors that governs fracture initiation, propagation, and fracture geometry during hydraulic stimulation.

In this study, we performed three test types on Freiberg gneiss core samples in the laboratory that include, hydrostatic and triaxial compression tests, ultrasonic velocity measurements, and oscillatory pore-pressure tests. The objectives of these laboratory tests were to deduce intrinsic rock properties and characterize their anisotropy based on the mechanical strength, elastic wave velocity, and hydraulic properties of the rocks recovered from the Freiberg mine site, as well as study their variation with stress. These results are valid for the behaviour of the rock surrounding Freiberg mine where hydraulic stimulation campaigns were performed and are expected to support conclusions made from the campaigns.

II. Material And Methods

Sample material

Mineralogical composition

Gneiss rock samples used in ultrasonic measurements and static tests were recovered at a depth of about 130-150 m from an abandoned silver mine in Freiberg, Germany. The main mineral composition is 33% of quartz, 37% of plagioclase and 17% of biotite. Other mineral present in the rock are muscovite and potassium feldspar (Jubelt, 1977). Another characteristic feature of the rock sample is the pronounced foliation (Fig. 1 a and b). The biotites form bulky elongated aggregates and produce an irregular striped pattern, foliation. The muscovites associate with biotites and appear to be newly formed. Plagioclases are part of the matrix and filled with mica felts. At the grain boundaries to potassium feldspar, plagioclases are prone to myrmekite formation. Potassium feldspar appears in large orthoclase porphyroblasts shown in greyish, bluish to light brownish interference colours (Fig. 1 c and d). Quartz can combine into large-scale grain aggregates and can also be found as small inclusions in the feldspars. Most of the gneiss is characterized by a granoblastic structure (Tichomirowa et al., 2001).

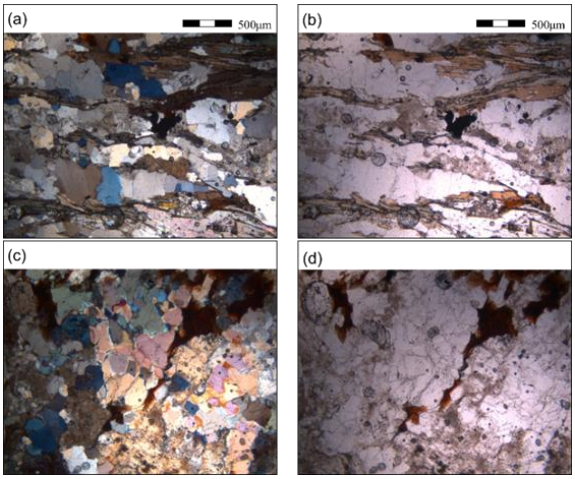

Figure 1. Thin section taken under cross-polarized light (a) parallel and (c) normal to the foliations, and plane-polarized light (b) parallel and (d) normal to the foliations.

Sample preparation

Samples of Freiberg gneiss with a diameter of 30 ± 0.05 mm were diamond-drilled in different orientations (0°, 30°, 45°, 60°, and 90°) relative to the visible foliation (Fig. 2). The end faces of each cored sample was smoothened flat by grinding to a final length of 75 ± 0.05 mm, resulting to a diameter-to-height ratio of 1:2.5, limiting the influence of the friction of steel pistons on the state of stress in the main part of the sample (Paterson & Wong, 2005). Coring, cutting, and grinding were done using water as a cooling fluid. Samples of each set of experiment were cored from the same rock block to minimize heterogeneity effect. Samples were characterized prior to testing by measuring basic physical properties.

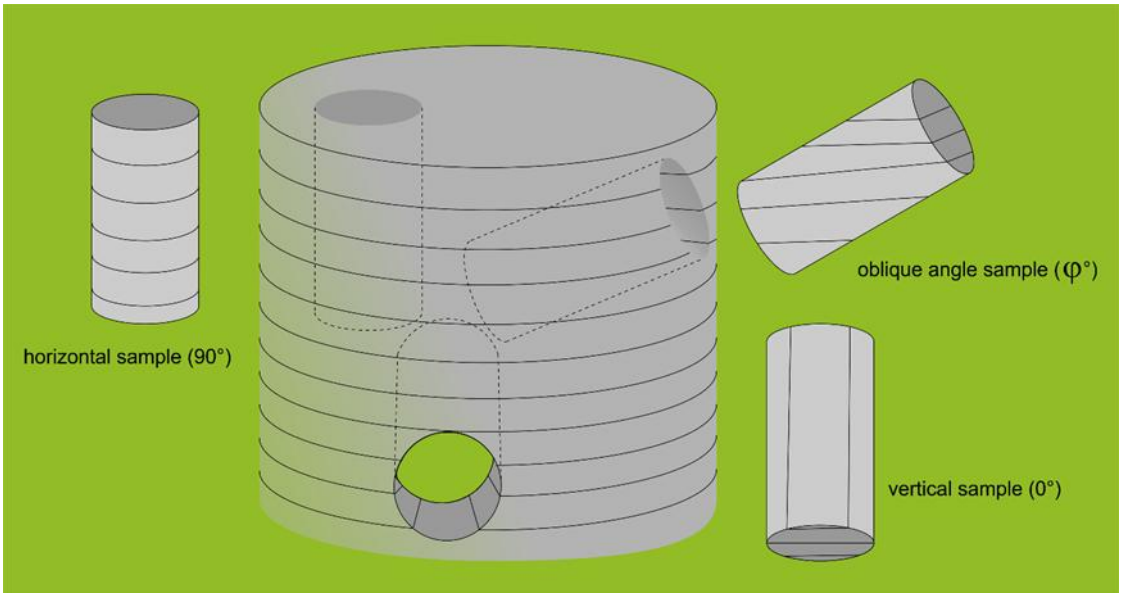

Figure 2. Reference scheme for sample orientation φ^{o}.

Basic physical properties at ambient conditions

The basic physical transport properties of the cylindrical gneiss samples at ambient conditions exhibit anisotropic characteristics. The axial propagation of P- and S-wave parallel to the plane of foliation is higher than propagation normal to the foliation plane. P-wave and S-wave velocities along vertical samples are higher than those of horizontal samples and P-wave and S-wave velocities of oblique angle samples are intermediate (Fig. 3 a and b). Additionally, P-wave and S-wave velocities of saturated samples are slightly higher than those of dry samples. The estimated compressional and shear wave anisotropy of dry samples is valued at 20 and 21% respectively. The ratio of P- to S- wave velocities for dry samples is approximately between 1.5 and 1.6 for all the sample orientations while the ratio for saturated samples is approximately between 1.5 and 1.7 (Fig. 3 c).

The dynamic moduli of the rock samples are also direction dependent with vertical samples exhibiting higher dynamic bulk and shear moduli than the horizontal samples (Fig. 3 d). The absence of a correlation between the P-wave and S-wave velocities and bulk density indicate that the cause for variability of velocity lies in structure rather than composition (Fig. 3 e). As expected, the volumetric properties are not direction dependent. However, values of total porosities are generally higher than those of effective porosities with highest variability in vertical samples (Fig. 3 f).

The basic physical properties of the cylindrical samples tested in this study vary both within the absolute measurement uncertainties and sample-to-sample variability. However, absolute measurement uncertainty is generally larger in most samples than uncertainty derived from sample-to-sample variability. Given that the samples were cored from the same rock block; the sample-to-sample variability is an indication that the Freiberg gneiss is not only anisotropic but also significantly heterogeneous.

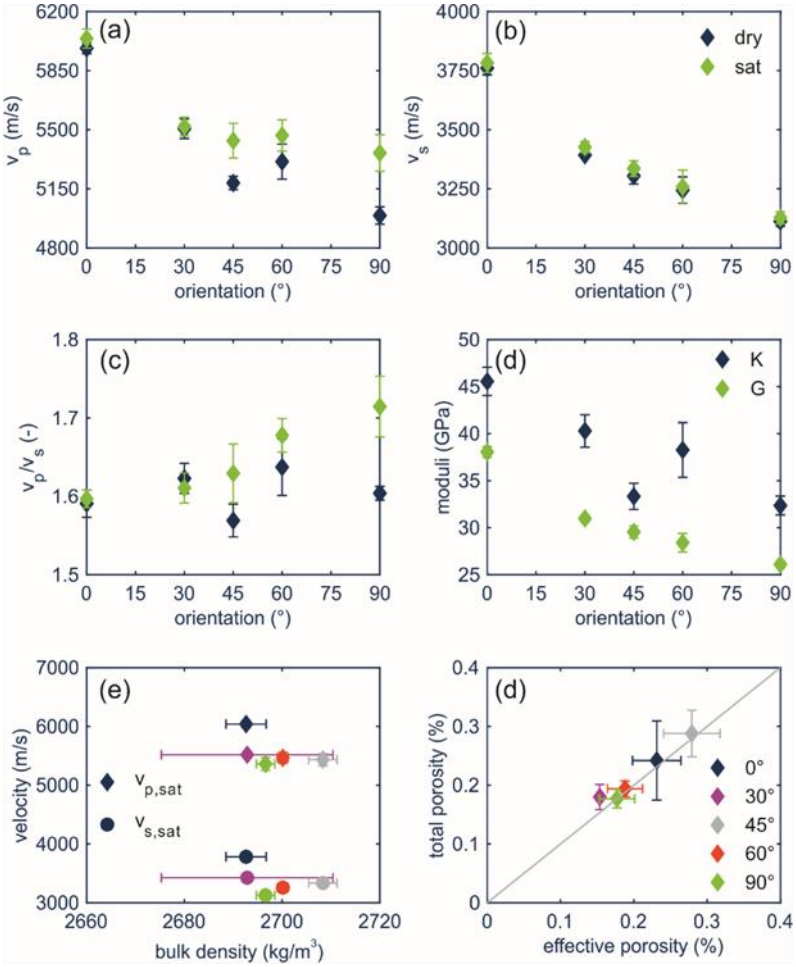

Figure 3. Ultrasonic (a) P-wave velocity of dry (blue) and saturated (green) samples, (b) S-wave velocity of dry and saturated samples, (c) v_p/v_s ratio of dry and saturated samples, (d) dynamic bulk (blue) and shear (green) moduli as functions of sample orientations, (e) ultrasonic P-wave velocity (diamond) and S-wave velocity (circle) as a function of bulk density and (f) total porosity as a function of effective porosity for different sample orientations. Different colors in plots (e) and (f) represent different rock sample orientations with respect to foliation. The error bars indicate the standard deviations establishing variability of the sample-to-sample of same orientation. The grey line represents a 1:1 line. All samples presented here were used for triaxial deformation tests.

Experimental apparatus and procedure

Hydraulic properties at different effective pressures

Hydraulic properties of Freiberg gneiss rock samples with different orientations relative to the foliation were determined using the conventional oscillatory pore-pressure method (Bernabe et al., 2005; Song & Renner, 2007; Suri, 1997), under hydrostatic loading at different effective pressures to investigate the pressure response of the low-porosity rock samples (<1 %) and the intact rock matrix anisotropy of hydraulic properties. The method involves the analysis of the pore-pressure signals at the *upstream* (top end of sample) transmitted axially through the rock sample and *downstream* (bottom end of sample) in terms of their amplitude differences and phase shifts.

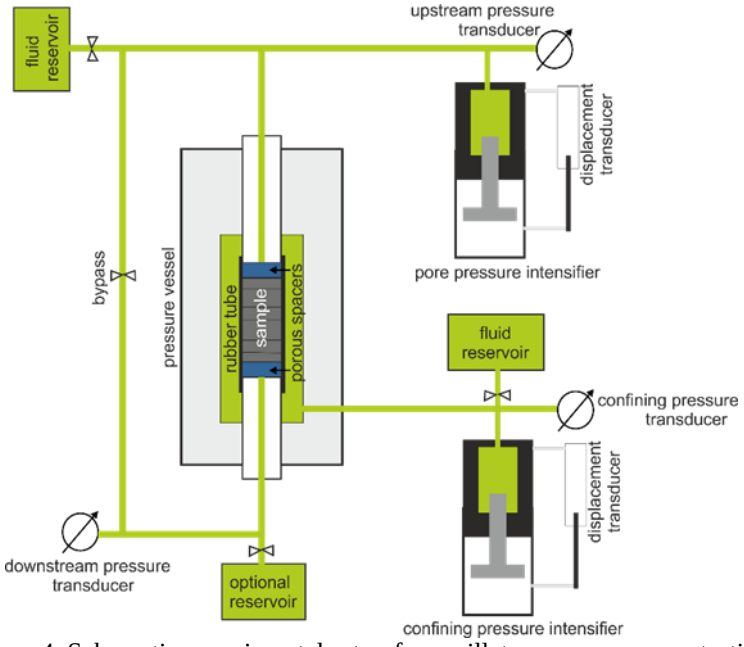

Figure 4. Schematic experimental setup for oscillatory pore pressure testing.

The experimental setup consists of a pore fluid system (distilled water), a confining fluid system (distilled water), and a control device (Fig. 4). The sample is jacketed using a rubber tube while mounted between the upstream and downstream reservoir to isolate the pore pressure fluid system from the confining pressure fluid system. Porous plates of known hydraulic properties are introduced, for even distribution of pore pressure, between the sample and the top and bottom platens. Two displacement and three pressure transducers measure the position of the intensifier pistons and the fluid pressures of the reservoirs and the vessel, respectively.

The pore-pressure oscillatory tests were performed on cylindrical samples with a diameter of 30 mm and a length of 25 mm. The shorter length was informed by the low-porosity nature of Freiberg gneiss and therefore, employing the scaling relation for a characteristic length $l_c \sim \sqrt{DT}$ to quantify the appropriate periods T with known diffusivity D that would necessitate the access to pore space and pressure response at the downstream during oscillatory test. The desired confining pressure was first applied to the sample followed by the pore pressure, then the sample was allowed to stabilize. A pore fluid pressure sinusoidal oscillation of period, ranging from 300 to 1500 s and amplitude maintained sufficiently low, at ~10% of the equilibrium pore pressure (to ensure that the rock and fluid properties were essentially constant during a particular measurement interval), was induced at the upstream. The equilibrium pore pressure was maintained at 1 MPa and consequently, the samples were tested for applied confining pressures of 2, 3 and 4 MPa resulting to effective pressures of 1, 2 and 3 MPa. During the oscillation interval, the upstream and downstream pressures were stored as a function of time for further evaluation of their amplitude ratio, phase shift and ultimate determination of hydraulic properties.

The method is based on the solution of one-dimensional diffusion equation for harmonic flow of a slightly compressible fluid and assumes a homogeneous and an isotropic porous medium (Fischer, 1992; Kranz et al., 1990). Permeability k and specific storage capacity s can be inverted from amplitude ratio and phase shift between the sinusoidal pore-pressure signal at the upstream and the corresponding pressure response signal at the downstream derived by Fourier analysis of the two signals. The analytic solution for homogeneous and isotropic sample gives amplitude ratio and phase shift as a function of the dimensionless storage (ξ) and transport (η) parameters (Bernabe, 2005), which are further related to specific storage capacity and permeability, respectively. A staggered grid search provides s and k values for ξ and η consistent with experimentally observed amplitude ratio and phase shift. The uncertainties in permeability, specific storage capacity and hydraulic diffusivity stem from the uncertainty in normalized parameters as a result of the variability in amplitude ratio and phase shift as well as accuracies of fluid viscosity, storage capacity of downstream reservoir, and dimensions of sample geometry.

Triaxial deformation tests

Conventional triaxial compression tests ($S_1 \geq S_2 = S_3$) without pore pressure were performed on dry samples in a pressure vessel using oil as confining fluid (Fig. 5). An axial load was applied to the sample at a steady rate by the axial loading pistons. The samples were assembled by placing porous spacers between the pistons and the end faces of the samples to ensure a uniform fluid pressure, and jacketed by rubber tubes before placing them in the pressure vessel. A high-pressure tube connected the vessel with a pressure transducer (accuracy 0.1%) and a pressure intensifier, referred to as bulk-volumometer. The bulk-volumometer was servo-hydraulically controlled using the displacement transducer (accuracy 0.1%) or pressure transducer. The axial load is measured with an external load cell (accuracy 0.01%), the axial displacement with a coupled pair of displacement transducers (accuracy 0.2%), an additional single displacement transducer (accuracy 0.1%), and the position of the bulk-volumometer piston with displacement transducer (accuracy 0.1%).

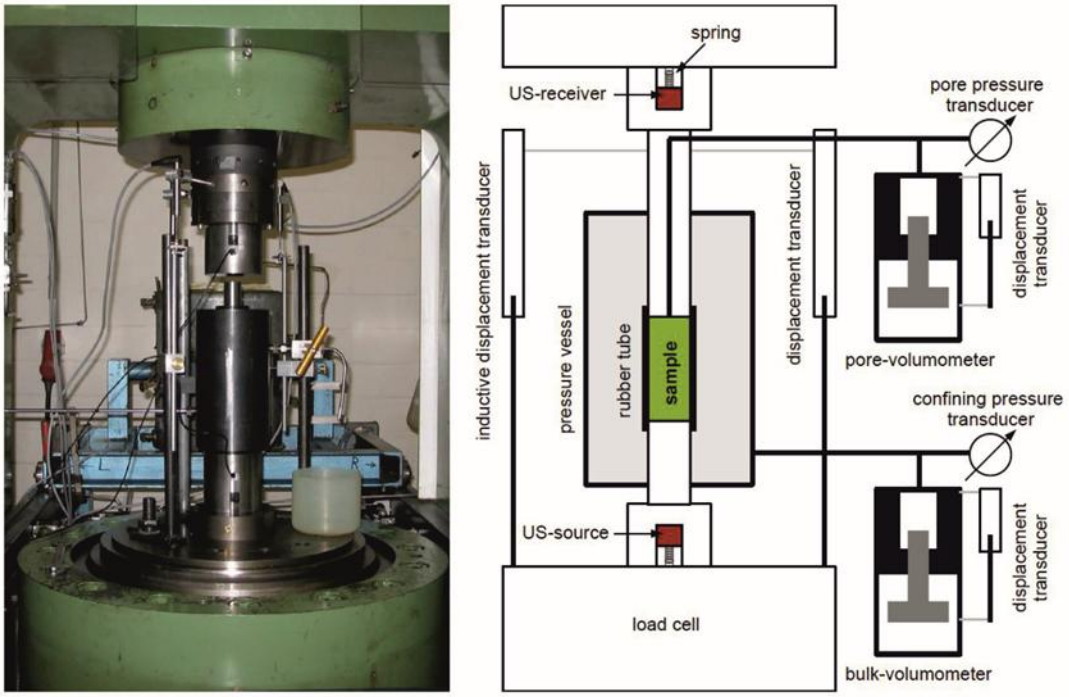

Figure 5. Photograph (left) and schematic experimental setup (right) for triaxial and hydrostatic compression tests with ultrasonic measurements (courtesy of Duda, 2011).

A suite of triaxial compression experiments was performed on the dry cylindrical samples of foliated Freiberg gneiss at five different confining pressures of 2.5 MPa, 5 MPa, 7.5 MPa, 10 MPa, and 12.5 MPa by superimposing an axial stress at each confining pressure, at an axial strain rate of 10^{-5} s^{-1}. The axial loading is displacement-controlled to avoid sudden sample failure around axial peak stress.

A pair of identical ultrasonic transducers with centre frequency of 1 MHz and diameter of 38.1 mm are positioned below and on top of the pressure vessel in line with axial loading pistons and are connected to the bench-top unit (Fig. 5). Ultrasonic travel times are continuously recorded every 60 s for the duration of the rock sample deformation to failure (each deformation experiment took about 20 minutes meaning about 20 waveforms were recorded). Analysis of the ultrasonic data during triaxial testing was performed according to Duda (2011) and Ahrens (2018). Prior to first arrivals picking, raw records were subjected to FFT bandpass filtering to remove low frequency bias (0 - 0.1MHz) and high frequency noise (1.2 – 2 MHz). A semi-automated method was used for the first arrival picking based on the similarity of the recorded signals. A reference arrival time was manually picked using the trace with the best signal-to-noise ratio from the first extremum value of the waveform corresponding to the direct P-wave propagating axially through the sample and assembly. Arrival times of all other recorded waveforms were then determined accounting for the time shift gained from two successive cross correlation performed between consecutive recorded signals. This technique detects the subtle changes in arrival time from one recorded waveform to the next facilitating the interpretation of velocity changes during deformation because they are not affected by the absolute uncertainty of velocity values.

Calibration experiment was performed on the steel sample in order to determine the effective travel time for the samples. This was achieved by subtracting travel time in the assembly from the total travel time

recorded. The correction accounted for the changes in length and P-wave velocity of the steel sample with increasing pressure and axial stress (Gerlich & Hart, 1984). Velocities were calculated by dividing the corrected sample lengths by the corrected transit times.

Hydrostatic deformation tests

Two series of hydrostatic compression experiments ($S_1 = S_2 = S_3 = p_c$) without pore pressure were performed in the triaxial deformation apparatus (Fig. 5) on intact Freiberg gneiss samples at confining pressures up to 10 MPa and 30 MPa, respectively, to establish stress-dependence of elastic wave velocity anisotropy. In the first hydrostatic experiment, travel times were recorded in 1 MPa increments between 0 and 10 MPa. Travel times of the second hydrostatic experiment were recorded in 3 MPa increment between 0 and 15 MPa, and in 5 MPa increments between 15 and 30 MPa during both the compression (loading) and decompression (unloading) cycles conducted at room temperature (21°C). The maximum confining pressure of 30 MPa exceeded the recreated in situ pressure (up to 5 MPa) conditions similar to those at depth to establish the pressure at which microcracks are closed. At each loading/unloading stage, the resultant P- and S-wave seismograms were recorded after stabilization of experimental apparatus (waveforms were recorded after waiting for 5 minutes to allow for thermal equilibration and pressure condition to stabilize in the pressure vessel). Thereafter, recorded seismograms were saved for further picking of first-arrival travel times and consequently determination of velocities. The loading cycle started with a confining pressure of 0 to 30 MPa followed by unloading cycle from 30 to 0 MPa at the rate of 0.045 MPa/min.

Calibration experiment was performed on hardened steel dummy with a Young's modulus of 210 GPa under the same experimental conditions as the test on rock samples to account for system stiffness and arrival times correction. Effective travel times for the samples were determined by subtracting the travel times in the assembly parts from the recorded travel times. The sample deformation occurring during hydrostatic compression/decompression though small (0.2%) for the range of pressures under investigation, was directly considered in the velocity calculation. Velocities were calculated as the ratios of corrected sample lengths (after accounting for shortening) to the corrected transit times (actual travel times through the samples). Expected uncertainties emanating from the sample geometry, accuracies of Young's modulus of steel (5%), accuracies of travel times (0.3%) resulted to absolute errors in P- and S-wave velocities values of less than 120 ms^{-1} and 80 ms^{-1}, respectively.

III. Results

Anisotropy of physical properties during elastic deformation

The results of deformation experiments, elastic velocities and hydraulic properties measurements, are presented during closing of micro-cracks at pressures below critical crack-closure pressure (hydrostatic compressions).

Hydraulic properties at different effective pressures

The tested intact Freiberg gneiss samples exhibit significant permeability anisotropy with maximum, intermediate, and minimum permeability recorded on vertical, oblique and horizontal samples, respectively (Fig. 6 a). Vertical sample permeability is about 5 times the horizontal sample permeability at the investigated effective pressures. Permeability and storage capacity tend to decrease with increasing effective pressure for all tested samples with horizontal sample showing the weakest pressure-sensitivity (Fig. 6 a and b). Vertical sample permeability at high effective pressure investigated (3 MPa) approaches the horizontal sample permeability. The closeness of permeabilities of horizontal sample and 45° sample demonstrates that the flow paths are strongly related to the foliation. The hydraulic diffusivity of the tested samples also shows direction-dependence with the vertical sample having higher hydraulic diffusivity than hydraulic diffusivity of the horizontal sample. The storage capacity and apparent porosity are nominally volumetric parameters, therefore are not direction-dependent, and their values are in the order of ~10^{-11} Pa^{-1} and ~10^{-2}, respectively (Fig. 6 c and d).

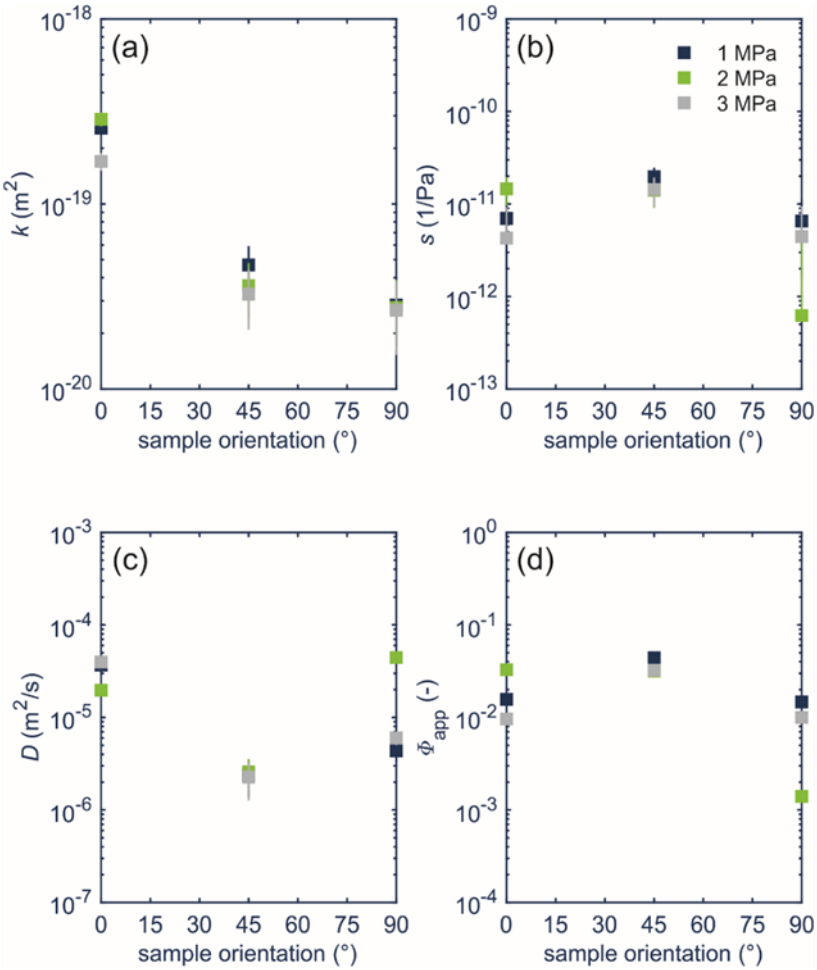

Figure 6. Variations in hydraulic properties with sample orientations for different effective pressures: (a) permeability, (b) storage capacity, (c) hydraulic diffusivity, and (d) apparent porosity.

Evolution of Elastic wave velocity during hydrostatic compression

Elastic wave velocities and anisotropy evolution during hydrostatic compression tests up to 10 MPa (Fig. 7 a) are shown for four distinct sample orientations (0°, 30°, 60°, and 90°). Freiberg gneiss being a foliated rock, samples undergo anisotropic mechanical compaction under increasing hydrostatic stress.

In the hydrostatic tests, the P- and S-waves travel at an increasing velocity with confining stress and exhibit velocity anisotropy. The increase in P- and S-wave velocities range from 1% for horizontal sample to 1.5% for vertical sample over the range of confining pressures of 0 to 10 MPa (

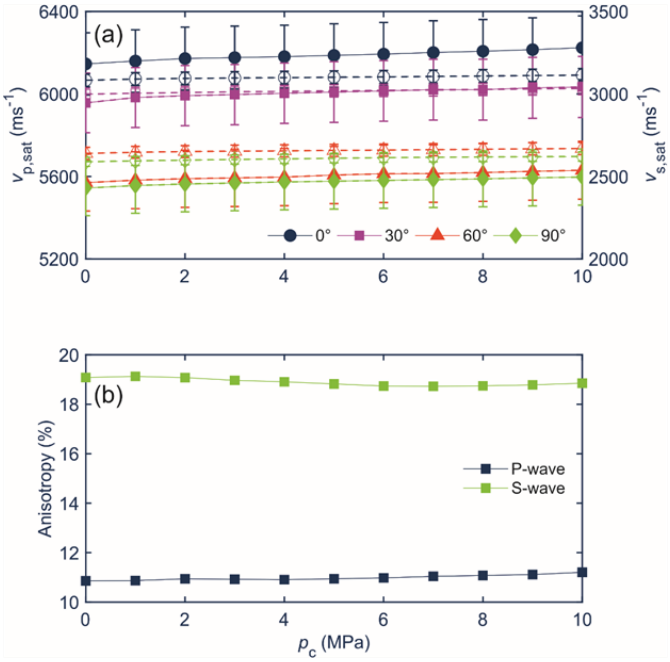

Figure a). However, this minimal increase is within the range of uncertainty of measurements. Similarly, for hydrostatic tests with range of confining pressures of up to 30 MPa, the increase in P-wave velocity below the confining pressure of 15 MPa occurs faster in horizontal samples by ~200 m/s compared to the P-wave velocity increase in vertical sample of ~80 m/s. Ultrasonic velocities for compressional and shear waves propagating parallel to the foliation (vertical sample) are higher than those propagating orthogonal to the foliation (horizontal sample). The following relation, $V_{p/s}(90°) < V_{p/s}(60°) < V_{p/s}(30°) < V_{p/s}(0°)$, is observed for velocity in Freiberg gneiss samples at all the investigated confining pressures. These rocks exhibit estimated average compressional and shear anisotropy values of 11 % and 19 %, respectively. Anisotropy changes minimally (0.2 %) over the range of confining pressures investigated for this experiment. The minimal change shows a decrease of compressional and shear anisotropy with confining pressure, however, this 0.2 % change is within the error of measurements (Fig. 7 b).

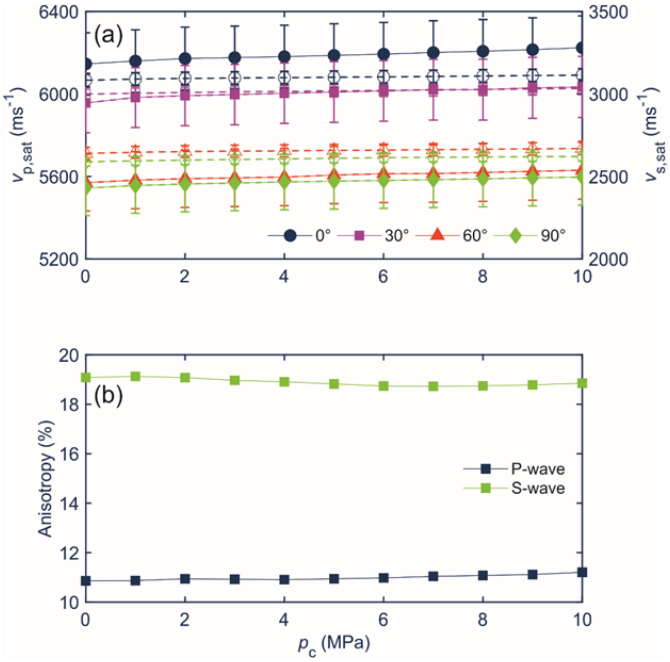

Figure 7. Evolution of (a) P-wave velocity (closed symbols) and S-wave velocity (open symbols) and (b) velocity anisotropy during hydrostatic compression up to 10 MPa confining pressure of saturated Freiberg gneiss samples with varying orientations relative to foliation.

Anisotropy of physical properties during inelastic deformation

The results of various tests that resulted to sample damage are presented to gain insights into the anisotropy of various mechanical properties during inelastic phase and their stress dependences.

Shear failure during triaxial deformation

In the range of confining pressures explored during triaxial compression experiments (0 to 12.5 MPa), the tested samples exhibit brittle failure with catastrophic axial stress drops after peak stress (Fig. 8 a and b). Volumetric strain of all samples initially increases indicating compaction, and reverses to dilation near the peak stress. Vertical and horizontal samples exhibit higher strengths and their dilation is much more pronounced than those of oblique-angle samples (30°, 45°, and 60) at all the explored confining pressures. The horizontal sample exhibits the highest volumetric strain and the vertical sample the least during initial compaction (Fig. 8b). The triaxial compression tests for vertical and horizontal samples reveal a prominent strength anisotropy of ~10 to 13%. Freiberg gneiss exhibits considerably higher compressive strengths when compressed with deformation axis normal to foliation compared to when the deformation axis is parallel to the foliation. In addition, the peak strength and residual strength increase with increasing confining pressure.

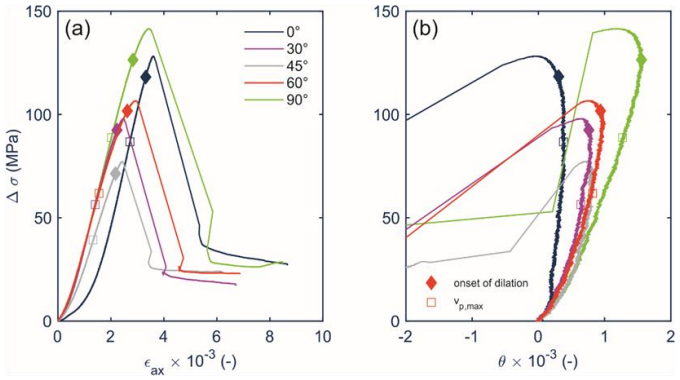

Figure 8. Axial stress difference plotted as a function of (a) axial strain and (b) bulk-volumetric strain during triaxial compression experiments on dry Freiberg gneiss of indicated five foliation orientations at effective confining pressure of 5 MPa. Diamond and square shapes give onset of dilation as deduced from bulk-volumetric strain and maximum P-wave velocity, respectively.

Evolution of P - wave velocity during triaxial deformation

P-wave velocity evolution during deviatoric loading may give insights into the micromechanics of deformation. P-wave velocity was measured for all the experiments during deformation, and here, we show the results for samples deformed at constant confining pressure of 5 MPa (Fig. 9). P-wave velocities increase with increasing axial strain and differential stress (Fig. 9 a and b) and reaches a maximum well before peak stress (Fig. 8). The change in velocity with increasing deviatoric stress and/or axial strain is more in the vertical sample than in the horizontal sample. At small differential stresses and axial strains, the rate of increase in P-wave velocity in most of the samples is relatively higher than at high differential stresses and axial strains. However, with increasing differential stress and axial strain, a decrease in the rate of increase in P-wave velocities is observed and subsequently, a distinct drop in velocity is observed at failure associated with the stress drop likely due to localised brittle failure, for all the sample orientations. The velocity anisotropy observed in the inelastic deformation including after failure is ~6%.

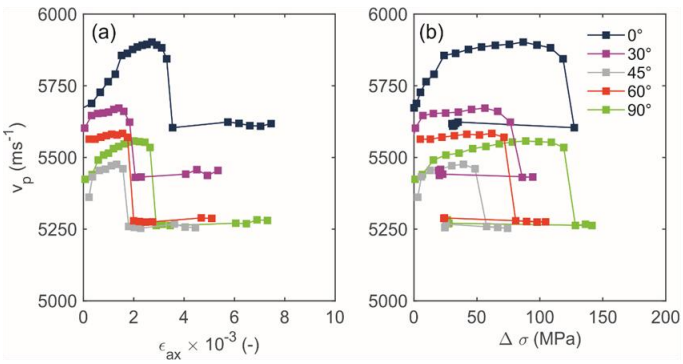

Figure 9. Evolution of P-wave velocity with (a) axial strain and (b) differential stress for experiment performed on Freiberg gneiss with different sample orientations at a confining pressure of 5 MPa.

The maximum P-wave velocity attained during deviatoric loading depends on the sample orientation and effective confining stresses (Fig. 10 a). However, the sample orientation (foliation) is dominant for the range of confining pressures explored. The maximum P-wave velocity attained during deviatoric loading of the vertical sample is significantly higher than the maximum velocity reached during deviatoric loading of horizontal sample. The maximum P-wave velocity attained for each tested sample slightly increases with increasing effective confining stress. Additionally, the maximum P-wave velocities attained during deviatoric loading for all the tested samples at the explored confining pressures are slightly higher than their counterpart velocities at hydrostatic pressures implying that at the onset of deviatoric loading, there is incomplete elastic closure of pre-existing cracks (Fig. 10 b).

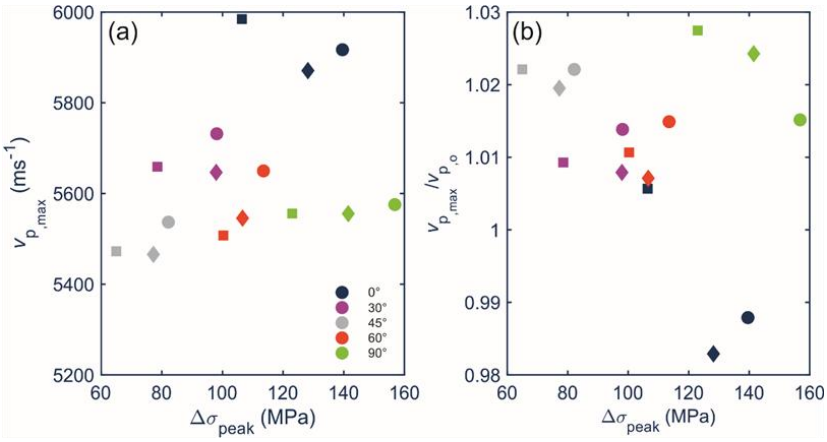

Figure 10. (a) Maximum P-wave velocity $v_{p,max}$ and (b) normalized maximum P-wave velocity $v_{p,max}/v_{p,o}$ as a function of peak differential stress $\Delta\sigma_{peak}$ for different sample orientations obtained during triaxial compression tests at effective confining pressures of 2.5 MPa (square shape), 5 MPa (diamond shape), and 7.5 MPa (circular shape). P-wave velocity is normalized by the initial P-wave velocity before deviatoric loading is applied.

IV. Discussion

Foliated metamorphic rock such as gneiss contain fabric with preferentially parallel arrangements of flat or long minerals. Foliation induced by the non-random orientation of minerals or micro-cracks leads to rock properties that are direction-dependent. Here, we discuss the correlations of different physical properties of Freiberg gneiss, permeability, wave velocity, tensile strength, and fracture toughness, relative to the foliation and the preferably oriented micro-cracks. Also, we investigate the relations between the foliation and oriented micro-cracks to shear failure and elastic wave propagational behaviour. Finally, a comparison of in-situ and laboratory ultrasonic velocity measurements is explained.

Correlation of directional physical properties

So far we have established that horizontal samples, i.e., cylinder axis is perpendicular to foliation, have higher initial crack porosity and density than vertical sample, i.e., cylinder axis is parallel to foliation. However, the results for permeability, which is pressure, crack and pore dependent, show that the permeability is larger/smaller for flow parallel/perpendicular to the foliation by about an order of magnitude (~10^{-19} m^2 vs. ~10^{-20} m^2) at an effective pressure of 1 MPa (Fig. 6 a). The sample permeability changes less significantly as a function of pressure but changes significantly as a function of flow direction relative to the orientation of the foliation. For the range of effective pressures applied in this study, pressure plays subordinate role to changes in permeability. At relatively high effective pressures of up to 80 MPa, Armitage (2011) and Gehne (2017) observed that permeability in both samples with foliation parallel and perpendicular to the cylinder axis change within the same order of magnitude, for their anisotropic sandstone samples. Micro-cracks and pores initially form a conductive pathway for fluid flow. In vertical sample, the axial fluid flow is parallel to foliation, the foliation and micro-cracks aligned with the foliation planes act as additional conduits for fluid flow, resulting to a better pressure response at the downstream, hence the relatively higher permeability than for fluid flow normal to the foliations in horizontal sample, where the foliation act as a barrier.

For the range of effective pressures tested, permeability anisotropy does not significantly change, suggesting that axial fluid flow is reduced by the same relative amount independent of flow direction. The permeability observations imply that pores and micro-cracks are elongated parallel to foliation, consistent with

the observations on the thin section, and therefore easy to close (Jones, 1998). The relatively high permeability exhibited by vertical sample compared to other samples may be explained as a series of high aspect ratio pores remaining open and therefore presenting additional flow paths in combination with foliation oriented parallel to the imposed oscillatory fluid flow. This flow path is however not present in horizontal sample, as the foliation present an additional barrier to the oscillatory fluid flow.

The knowledge of stress path and evolution of permeability in varied direction is particularly applicable in field cases involving laminated rocks, such as shale, and how they respond to hydraulic stimulation (Gehne, 2017). The tested Freiberg samples exhibit higher initial permeability anisotropy than elastic wave velocity anisotropy. However, the directions of the maximum and minimum flow are in good agreement with the principal directions of wave propagation indicated by velocities. This observation is consistent with permeability experiments with simultaneous elastic wave velocity measurements performed on different rock samples from literature (Benson et al., 2005; Benson et al., 2006; Gehne, 2017).

Generally, permeability and elastic wave velocity of Freiberg gneiss are slightly pore and micro-crack dependent, but prominently foliation dependent (Fig. 11). Relatively, high permeability and velocity are exhibited in the direction parallel to the foliation (direction of maximum flow) as compared to the direction perpendicular to the foliation.

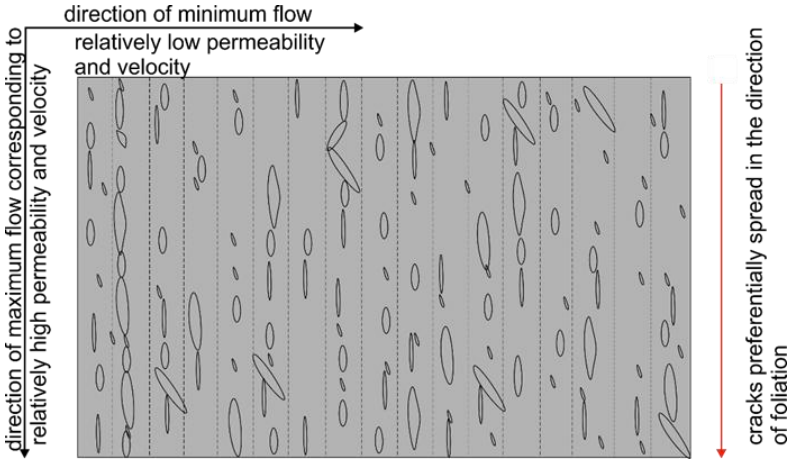

Figure 11. Schematic representation of Freiberg gneiss indicating foliation (broken line) and micro-cracks (elliptical shapes) generally oriented parallel to foliation. The correlations of directional physical properties are indicated relative to the principle directions.

Effect of gneiss foliation on shear failure

Before the formation of a macroscopic fracture leads to failure of a rock, microscopic cracks form when locally critical stresses are exceeded (Jaeger, 2007; Tapponnier & Bracet, 1976). Freiberg gneiss undergo brittle failure at the investigated pressures, resulting to formation of brittle fractures. In brittle failure, immediately after elastic deformation phase, nucleation and growth of stress-induced cracks occur, at low angles (less than 45°) to the maximum principal stress. These cracks eventually grow to a length comparable to their spacing and interact with one another, leading to macroscopic fault formation and failure (Rawling et al., 2002; Wong, 1982).

The results of our triaxial compression tests demonstrate that the foliation is associated with planes. For samples with the foliation 30° to 60° relative to the cylinder axis, the fracture plane coincides with foliation planes (Fig. 12 c, d and e) and these samples fail at lower stresses (less than 120 MPa) than either samples whose axes are 0° or 90° to the foliation, at the maximum confining pressure investigated. A single shear fault plane was observed in the deformed Freiberg gneiss with foliation between 30° to 60° relative to cylinder axis. The fault planes appeared fairly smooth and dominated by sheet silicates, a constituent mineral making up the foliation. These observations on fault morphology correlate well with the characteristics of the stress-strain curves exhibiting a transition from high peak stresses for non-sliding failure (failure within the rock matrix) to relatively low peak stresses for sliding failure (failure on the foliation) at all the confining pressures explored.

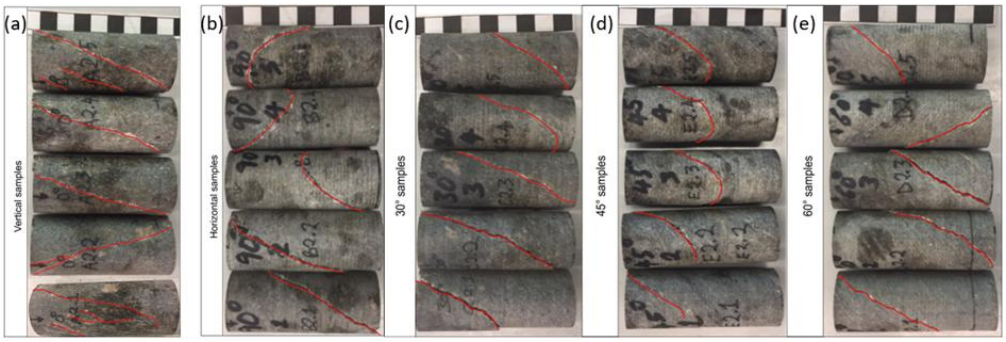

Figure 12. Deformed samples of 30° (top), 45° (middle) and 60° (down) oriented samples relative to core axis retrieved from the pressure vessel after triaxial deformation tests.

The horizontal samples (90°) do not fracture in the direction of foliation, but at less than 45° from the direction of maximum principle stress, partly because the load acts perpendicular to the foliation thus inhibiting fracturing parallel to the foliation or that the foliation is not at the optimal orientation for shear failure (Fig. 12 b). The deformed vertical samples (0°) show partial axial splitting in the direction of the foliation (Fig. 12 a). For these samples, the alignment of foliation with direction of axial stress is likely to promote the nucleation of micro-cracks along the foliation. Micro-cracks initially propagate at low angle to the maximum principal stress, an optimal orientation for shear failure of rock matrix, but then deviate when encountering foliation, i.e., acting as a weak plane (Gehne, 2017).

Anisotropy in elastic wave velocity during deformation

P- and S-wave velocity of the most common metamorphic rocks can often be described as transversely isotropic (Barberini et al., 2007). Using the inversion results for Thomsen's parameters δ, ε, and γ for a transversely isotropic velocity model (Thomsen, 1986), we can predict velocities along propagation directions that were not measured experimentally. For instance, we observe during the hydrostatic compression (Fig. 13 a and b) the increase of P- and S-wave velocity from about 5650 m/s to 5750 m/s and 2910 m/s to 2980 m/s, respectively, for waves propagating at an angle of 45° to the foliation.

The anisotropy in rocks is primarily due to the preferred orientation of the constituent minerals, textural-structural features, pores, and cracks (Chan, 2015; Heng et al., 2015; Ki et al., 2017; Özbek et al., 2018). The effects of micro-cracks and pores on rock anisotropy is expected to decline with applied increasing confining pressure, and the remaining anisotropy is more likely resulting from layering and preferred orientation of minerals, i.e., intrinsic anisotropy. Subsequently, closing of the cracks in turn results in the increase of P- and S-wave velocities (Walsh, 1965).

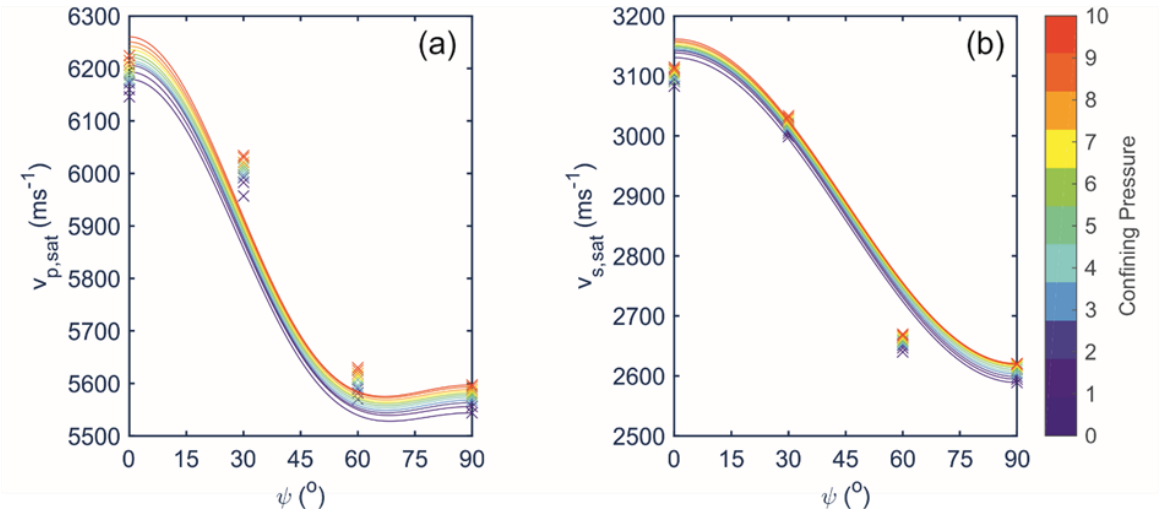

Figure 13. Evolution of saturated (a) P-wave velocity $V_{p,sat}$ and (b) S-wave velocity $V_{s,sat}$ during hydrostatic deformation up to 10 MPa for different sample orientations ψ. The solid lines correspond to the shape of the saturated P- and S-wave velocity evolution calculated from the inverted Thomsen's parameters using the measured values plotted with symbols. Colour scale is related to confining pressure.

P- and S-wave velocities parallel to the foliation plane are greater than those in the perpendicular and oblique directions. The relatively small increase in P- and S-wave velocities (< 2 %) at confining pressures of up to 10 MPa, may suggest that velocities are not significantly controlled by the micro-cracks. As the confining pressures increases beyond critical crack-closure pressure, layering and the preferred orientation of minerals are expected to have dominant effects on the anisotropic behaviour of the rock as opposed to the cracks. Microscopic analysis of the thin sections of the rock sample seems to fairly verify this interpretation with the presence of micro-cracks and aggregates of elongated biotite oriented in the same direction (Fig. 1). This observation is true for both hydrostatic and triaxial compression experiments. The foliation seems to be the dominant factor contributing to the anisotropy of elastic velocities in Freiberg gneiss and not micro-cracks and pores because the observed anisotropy at ambient pressure does not significantly change during hydrostatic compressions.

During triaxial compression tests at different confining pressures, the changes in P-wave velocity during deviatoric loading is high in the horizontal sample than in the vertical sample, further attesting to the sensitivity of horizontal sample to pressure (Fig. 10 b). When the samples approach failure, P-wave velocity shows a marked decrease, suggesting the proliferation of cracks in the samples, consistent with onset of dilation. According to experiments performed with acoustic emission sensors in the literature, at this stage, micro-cracks could be localized, and macroscopic shear fractures could form (e.g., Lockner et al., 1992; Schubnel et al., 2003).

Comparisons of field in-situ velocity with laboratory ultrasonic velocity measurements

The variability in velocity exhibited in the laboratory results for samples from different blocks tested in the same orientation, increases from foliation parallel (0°) to foliation perpendicular (90°) from about 5 to almost 20% (Fig. 3 e). There is no obvious correlation with density, implying the cause for variability lies in structure rather than composition. The average compressional velocity anisotropy obtained from the laboratory measurements is about 20%. The foliation in the Freiberg mine test-volume is sub-horizontal, and according to Boese et al. (2022) the in-situ P-wave velocity increases from vertical to horizontal corresponding to compressional velocity anisotropy of ~20% (Fig. a and b), consistent with the compressional velocity anisotropy obtained from the laboratory. Despite the differences in frequency bands of ultrasonic velocity transmission sources in the laboratory (500 kHz – 800 kHz) and in the field scale (< 100 kHz), good correspondence between in-situ and laboratory velocity results was observed (Fig. 14 b). This consistency in velocity is unexpected because laboratory ultrasonic measurements are performed on intact rock samples of centimetre size while the in-situ ultrasonic measurements are performed on a test-volume of decametre size containing joints and fractures with a linear fracture density as high as 5 m^{-1} (Adero, 2020).

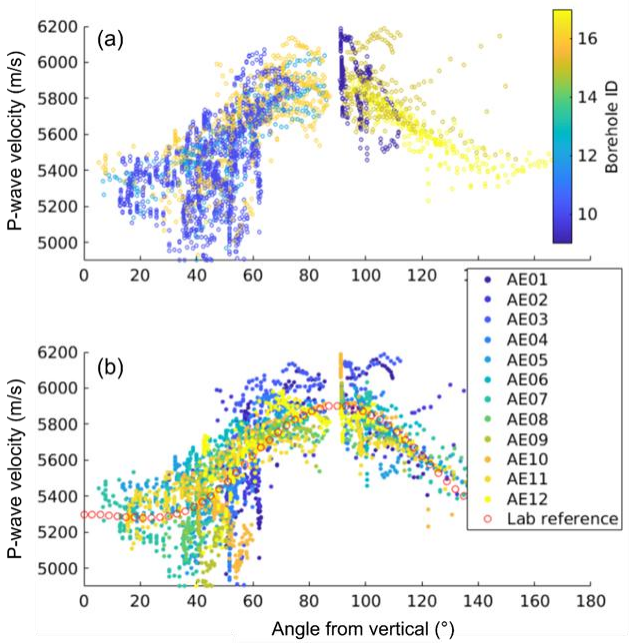

Figure 14. Variability of P- wave velocity with angle from vertical of the tunnel measured using an array of acoustic emission sensors in the Freiberg test-volume with (a) reference to the boreholes, and (b) acoustic emission sensors, correlated with P-wave velocities determined from the laboratory (red circle). (Field data courtesy of Boese, (2022)).

To understand this consistency in the laboratory and field velocity, we applied our laboratory velocity measurements into a model of seismic wave transmission across a fracture proposed by Pyrak-Nolte et al. (1990) to obtain transmitted wave group-time delay t_{gr} according to

$$t_{gr} = 2(K_s / Z) / [4(K_s / Z)^2 + \omega^2] \qquad (0.1)$$

where K_s, Z, and ω denote normal stiffness of the fracture, seismic impedance of the intact material derived from the product of density and velocity, and frequency, respectively. We assume that the P-wave propagates normal to the fracture and for simplicity that the fracture network in the rock mass is represented by a single discontinuity with effective stiffness between 10^8 to 10^{11} Pa/m, subsuming the contribution of the 10 to 100 fractures on a wave path. According to the model, a significant transmitted wave group-time delay is depicted for stiffnesses between 10^{10} to 10^{11} Pa/m, i.e., greater than 4 μs, for frequencies in the laboratory and field measurements, implying different observations (Fig. 15). However, with the range of fracture stiffness between 10^8 to 10^9 Pa/m, the observations from the laboratory and field coincide despite their frequency differences, considering relatively smaller transmitted wave group-time delay (<1 μs).

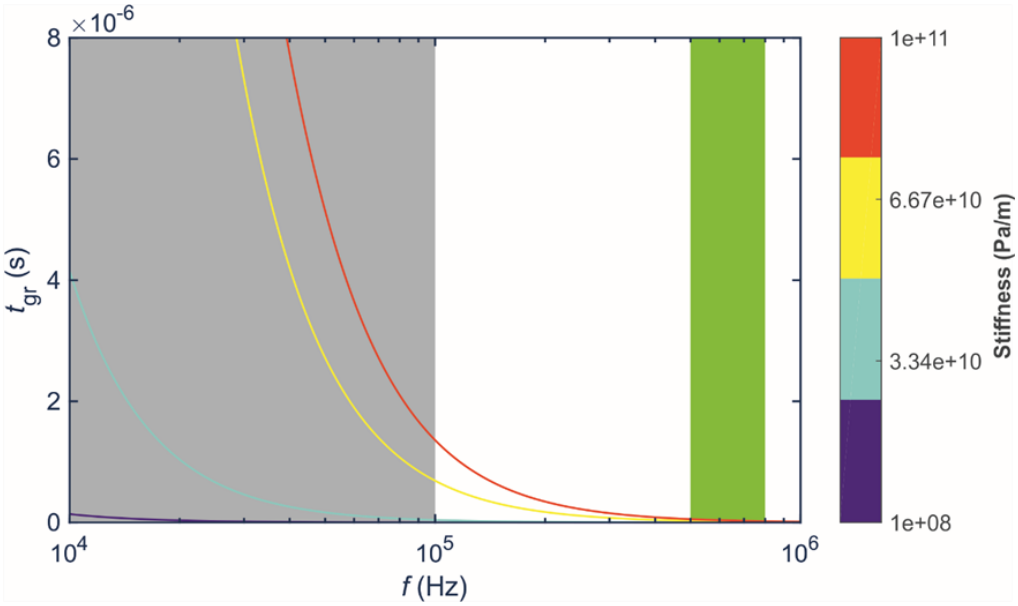

Figure 15. Transmitted wave group time delay t_{gr} as a function of frequency f for the limit of fracture stiffnesses shown by the colorbar. The grey and green stripes on the left and on the right show the frequency band of the in-situ and laboratory velocity measurements, respectively.

V. Conclusion

Foliation and micro-cracks with preferred orientations are sources of directional dependency of elastic, mechanical and hydraulic properties of Freiberg gneiss. The extensive laboratory anisotropy characterisation of the Freiberg gneiss is summarized as follows:

- The tested rock showed significant mechanical anisotropy with samples deformed normal to the foliation exhibiting higher mechanical strengths than samples deformed parallel to the foliation. The shear failure of the oriented samples was characterised by a smooth strength variation with loading direction. Failure along weak plane, that is foliation, was exhibited by the characteristic sudden decrease in strength for specific ranges of rock sample orientation relative to the loading direction. Specifically, the compressive strength of Freiberg gneiss was weakest at 45° where the rock samples failed by sliding along the foliation plane.
- The effect of stress on elastic properties is often dominated by the existence of micro-cracks that diminishes as stress is increased. However, the anisotropy in elastic wave velocity of Freiberg gneiss is dominated by the foliation and not micro-cracks. The velocity anisotropy does not significantly change with both hydrostatic and deviatoric stress loading. In addition, the intact Freiberg gneiss rock mass is generally stiff, considering the value of its Young's modulus (> 50 GPa), and the stiffness of the fractures within the rock mass is ~ 1 % of the stiffness of intact rock, thus, the consistency in the elastic wave velocities measured in the laboratory and in the field.

- The anisotropy in rock matrix permeability of Freiberg gneiss can be partially due to, to a small extent, an artefact of existence of micro-cracks and predominantly due to the foliation heterogeneity when the oriented samples are tested. The permeability in the direction of the foliation is higher than permeability perpendicular to the foliation by at least an order of magnitude. The changes in stress do not significantly affect permeability.

Acknowledgement

I am grateful to Professor Jörge Renner from Ruhr University Bochum who was my doctoral supervisor for his guidance during my study.

Funding Source

The author gratefully acknowledges the funding provided by the German Federal Ministry of Education and Research (BMBF) for the STIMTEC project (subprojects HYSPALAB, Grant numbers 03A0015A).

References

[1]. Adero, B. (2020). Experimental investigations of mechanical anisotropy of Freiberg gneiss: implications for hydraulic stimulation. Ruhr-Universität Bochum.

[2]. Ahrens, B., Duda, M., & Renner, J. (2018). Relations between hydraulic properties and ultrasonic velocities during brittle failure of a low-porosity sandstone in laboratory experiments. Geophysical Journal International, 212(1), 627–645. https://doi.org/10.1093/gji/ggx419

[3]. Armitage, P. J., Faulkner, D. R., Worden, R. H., Aplin, A. C., Butcher, A. R., & Iliffe, J. (2011). Experimental measurement of, and controls on, permeability and permeability anisotropy of caprocks from the CO<inf>2</inf> storage project at the Krechba Field, Algeria. Journal of Geophysical Research: Solid Earth, 116(12), 1–18. https://doi.org/10.1029/2011JB008385

[4]. Barberini, V., Burlini, L., & Zappone, A. (2007). Elastic properties , fabric and seismic anisotropy of amphibolites and their contribution to the lower crust reflectivity. Tectonophysics, 445, 227–244. https://doi.org/10.1016/j.tecto.2007.08.017

[5]. Baud, P., Meredith, P., & Townend, E. (2012). Permeability evolution during triaxial compaction of an anisotropic porous sandstone. Journal of Geophysical Research: Solid Earth, 117(5), 1–23. https://doi.org/10.1029/2012JB009176

[6]. Benson, M., Meredith, G., & Schubnel, A. (2006). Role of void space geometry in permeability evolution in crustal rocks at elevated pressure. Journal of Geophysical Research, 111(December), 1–14. https://doi.org/10.1029/2006JB004309

[7]. Benson, P. M., Meredith, P. G., Platzman, E. S., & White, R. E. (2005). Pore fabric shape anisotropy in porous sandstones and its relation to elastic wave velocity and permeability anisotropy under hydrostatic pressure. International Journal of Rock Mechanics & Mining Sciences, 42, 890–899. https://doi.org/10.1016/j.ijrmms.2005.05.003

[8]. Bernabe, Y., Mok, U., & Evans, B. (2005). A note on the oscillating flow method for measuring rock permeability ´. International Journal of Rock Mechanics and Mining Sciences, 43(2006), 311–316. https://doi.org/10.1016/j.ijrmms.2005.04.013

[9]. Bhandari, A. R., Flemings, P. B., Polito, P. J., Cronin, M. B., & Bryant, S. L. (2015). Anisotropy and Stress Dependence of Permeability in the Barnett Shale. Transport in Porous Media, 108, 393–411. https://doi.org/10.1007/s11242-015-0482-0

[10]. Boese, C. M., Kwiatek, G., Fischer, T., Plenkers, K., Starke, J., Blümle, F., … Dresen, G. (2022). Seismic monitoring of the STIMTEC hydraulic stimulation experiment in anisotropic metamorphic gneiss. Solid Earth, 13(2), 323–346. https://doi.org/10.5194/se-13-323-2022

[11]. Bradehoeft, J. D., England, A. W., Stewart, D. B., Traske, N. J., & Winograd, I. J. (1978). Geologic Disposal of High-Level Radioactive Wastes. Earth Science Perspectives. U.S. Geol. Surv., Circ.,779: 15.

[12]. Chan, J., & Schmitt, D. R. (2015). Elastic Anisotropy of a Metamorphic Rock Sample of the Canadian Shield in Northeastern Alberta. Rock Mechanics and Rock Engineering, 48(4), 1369–1385. https://doi.org/10.1007/s00603-014-0664-z

[13]. David, C., Menendez, B., & Zhu, W. (2001). Mechanical Compaction, Microstructures and Permeability Evolution in Sandstones, (1), 45–51.

[14]. Donath, F. A. (1961). Short Notes, (June).

[15]. Duda, M. (2011). An integrated experimental study on elastic and inelastic properties of sandstones and the role of transient pore pressure . Dissertation, Ruhr Universität Bochum.

[16]. Fischer, G. J. (1992). The determination of permeability and storage capacity pore pressure oscillation method.pdf. In Fault Mechanics and Transport Properties of Rocks (pp. 187–211). San Diego: Academic Press.

[17]. Fryer, B., Siddiqi, G., & Laloui, L. (2019). Compaction-Induced Permeability Loss ' s Effect on Induced Seismicity During Reservoir Depletion. Pure Appl. Geophys, 176, 4277–4296. https://doi.org/10.1007/s00024-019-02198-0

[18]. Gehne, S., & Benson, P. M. (2017). Permeability and permeability anisotropy in Crab Orchard sandstone: Experimental insights into spatio-temporal effects. Tectonophysics, 712–713, 589–599. https://doi.org/10.1016/j.tecto.2017.06.014

[19]. Gerlich, D., & Hart, S. (1984). Pressure dependence of the elastic moduli of three austenitic stainless steels. Journal of Applied Physics, 55(4), 880–884. https://doi.org/10.1063/1.333138

[20]. Heng, S., Guo, Y., Yang, C., Daemen, J. J. K., & Li, Z. (2015). International Journal of Rock Mechanics & Mining Sciences Experimental and theoretical study of the anisotropic properties of shale. International Journal of Rock Mechanics and Mining Sciences, 74, 58–68. https://doi.org/10.1016/j.ijrmms.2015.01.003

[21]. Hofmann, H., Blöcher, G., Börsing, N., Maronde, N., Pastrik, N., & Zimmermann, G. (2014). Potential for enhanced geothermal systems in low permeability limestones – stimulation strategies for the Western Malm karst (Bavaria). Geothermics, 51, 351–367. https://doi.org/10.1016/j.geothermics.2014.03.003

[22]. Ismael, M. A., Imam, H. F., & El-shayeb, Y. (2014). Journal of Rock Mechanics and Geotechnical Engineering A simpli fi ed approach to directly consider intact rock anisotropy in Hoek e Brown failure criterion. Journal of Rock Mechanics and Geotechnical Engineering, 6(5), 486–492. https://doi.org/10.1016/j.jrmge.2014.06.003

[23]. Jaeger, J. C., Cook, N. G., & Zimmerman, R. W. (2007). Fundamentals of Rock Mechanics (Fourth). Blackwell Publishing.

[24]. Jones, C. (1998). An experimental study of elastic wave propagation anisotropy and permeability anisotropy in an illitic shale. SPE/ISRM Rock Mechanics in Petroleum Engineering.

[25]. Kim, H., Xie, L., Min, K. B., Bae, S., & Stephansson, O. (2017). Integrated In Situ Stress Estimation by Hydraulic Fracturing, Borehole Observations and Numerical Analysis at the EXP-1 Borehole in Pohang, Korea. Rock Mechanics and Rock Engineering, 50(12), 3141–3155. https://doi.org/10.1007/s00603-017-1284-1

[26]. Kranz, R. L., Saltzman, J. S., & Blacic, J. D. (1990). Hydraulic Diffusivity Measurements on Laboratory Rock Samples Using an Oscillating Pore Pressure Method. Int. J. Rock Mech. Min. Sci. & Geomech. Abstr., 27(5), 345–352.

[27]. Lockner, D. A., Byerlee, J. D., Kuksenko, V., Ponomarev, A., Sidorin, A., Survey, U. S. G., … Park, M. (1992). Observations of Quasistatic Fault Growth from Acoustic Emissions. Fault Mechanics and Transport Properties of Rocks. San Diego, CA: Academic Press.

[28]. Marek, B. F. (1979). Permeability loss in depletion of reservoirs. In 5th. Annu. Conf., Society of Petroleum Engineers (Vol. 5, p. SPE pap. 8433). Las Vegas, NV.

[29]. Niandou, H., Shao, J. F., Henry, J. P., & Fourmaintraux, D. (1997). Laboratory investigation of the mechanical behaviour of Tournemire shale. International Journal of Rock Mechanics and Mining Sciences, 34(1), 3–16. https://doi.org/10.1016/S1365-1609(97)80029-9

[30]. Özbek, A., Gül, M., Karacan, E., & Alca, Ö. (2018). Journal of Rock Mechanics and Geotechnical Engineering Anisotropy effect on strengths of metamorphic rocks. Journal of Rock Mechanics and Geotechnical Engineering, 10(1), 164–175. https://doi.org/10.1016/j.jrmge.2017.09.006

[31]. Paterson, M. S., & Wong, T. (2005). No Title. Berlin Heidelberg: Springer Verlag.

[32]. Pyrak-Nolte, L. J., Myer, L. R., & Cook, N. G. (1990). Transmission of seismic waves across single natural fractures. Journal of Geophysical Research, 95(B6), 8617–8638.

[33]. Rawling, G. C., Baud, P., & Wong, T. (2002). Dilatancy, brittle strength, and anisotropy of foliated rocks: Experimental deformation and micromechanical modeling. Journal of Geophysical Research: Solid Earth, 107(B10), ETG 8-1-ETG 8-14. https://doi.org/10.1029/2001jb000472

[34]. Saroglou, H. Ã., & Tsiambaos, G. (2008). A modified Hoek – Brown failure criterion for anisotropic intact rock, 45, 223–234. https://doi.org/10.1016/j.ijrmms.2007.05.004

[35]. Sarout, J., & Guéguen, Y. (2008). Anisotropy of elastic wave velocities in deformed shales: Part 1—Experimental results. Geophysics, 73(5), D75–D89. https://doi.org/10.1190/1.2952744

[36]. Sayers, C. M. (2013). The effect of anisotropy on the Young's moduli and Poisson's ratios of shales. Geophysical Prospecting, 61(2), 416–426. https://doi.org/10.1111/j.1365-2478.2012.01130.x

[37]. Schubnel, A. S., Ishizawa, O. N., & Asuda, K. M. (2003). Velocity Measurements and Crack Density Determination During Wet Triaxial Experiments on Oshima and Toki Granites, 160, 869–887.

[38]. Song, I., & Renner, J. (2007). Analysis of oscillatory fluid flow through rock samples, 195–204. https://doi.org/10.1111/j.1365-246X.2007.03339.x

[39]. Suri, P., Azeemuddin, M., Zaman, M., Kukreti, A. R., & Roegiers, J. (1997). Stress-dependent permeability measurement using the oscillating pulse technique, 17, 247–264.

[40]. Tapponnier, P., & Bracet, W. F. (1976). Development.of Stress-Induced Mlcrocracks m Westerly Granite. Int. J. Rock Mech. Min. Sci. & Geomech. Abstr, 13, 103–112.

[41]. Terzaghi, K. (1943). Theoretical Soil Mechanics. https://doi.org/10.1002/9780470172766

[42]. Tester, J. W., Anderson, B. J., Batchelor, A. S., Blackwell, D. D., DiPippo, R., Drake, E. M., … Richards, M. (2006). The Future of Geothermal Energy - Impact of Enhanced Geothermal Systems (EGS) on the United States in the 21st Century.

[43]. Thomsen, L. (1986). Weak elastic anisotropy. Geophysics, 51(October), 1954–1966.

[44]. Tichomirowa, M., Berger, H., Koch, E. A., Belyatski, B. V, & Gotze, J. (2001). Zircon ages of high-grade gneisses in the Eastern Erzgebirge (Central European Variscides) — constraints on origin of the rocks and Precambrian to Ordovician magmatic events in the Variscan foldbelt. Elsevier Lithos, 56, 303–332.

[45]. Walsh, J. B. (1965). The Effect of Cracks on the Compressibility of Rock. Journal of Geophysical Research, 70(2), 381–389.

[46]. Walsh, J. B., & Brace, W. F. (1964). A Fracture Criterion for Brittle Anisotropic rock. Journal of Geophysical Research, 69(16), 3449–3456.

[47]. Wong, T. F. (1982). Micromechanics of faulting in westerly granite. International Journal of Rock Mechanics and Mining Sciences And, 19(2), 49–64. https://doi.org/10.1016/0148-9062(82)91631-X

[48]. Zharikov, A. V, Velichkin, V. I., Malkovsky, V. I., & Shmonov, V. M. (2014). Experimental Study of Crystalline Rock Permeability : Implications for Underground Radioactive Waste Disposal, 41(7), 881–895. https://doi.org/10.1134/S0097807814070136